

# Temperature and Vibration Insensitive Fiber-Optic Current Sensor

K. Bohnert, *Member, OSA*, P. Gabus, J. Nehring, and H. Brändle

**Abstract**—A robust interferometric fiber-optic current sensor with inherent temperature compensation of the Faraday effect is presented. Sensor configurations based on Sagnac and polarization-rotated reflection interferometers are considered. The sensing fiber is residing and thermally annealed in a coiled capillary of fused silica. The capillary is embedded in silicone within a ring-shaped housing. It is theoretically and experimentally shown that the temperature dependence of the birefringent fiber-optic phase retarders of the interferometers can be employed to balance the temperature dependence of the Faraday effect ( $0.7 \times 10^{-4}/^\circ\text{C}$ ). Insensitivity of the sensor to temperature within 0.2% is demonstrated between  $-35^\circ\text{C}$  and  $85^\circ\text{C}$ . The influence of the phase retarders on the linearity of the sensor is also addressed. Furthermore, the sensitivity to vibration of the two configurations at frequencies up to 500 Hz and accelerations up to 10 g is compared. High immunity of the reflective sensor to mechanical perturbations is verified.

**Index Terms**—Current measurement, Faraday effect, nonreciprocal wave propagation, optical fiber devices, optical fiber transducers, optical interferometry, optical phase shifters.

## I. INTRODUCTION

CURRENT sensors employing the Faraday effect in a coil of optical fiber are very attractive for metering, control, and protection in high-voltage substations. Advantages include the inherent electric separation of the sensor electronics at ground potential from the sensing fiber coil at high voltage as well as the small size and weight. As a result, the sensors can be integrated into existing high-voltage equipment such as circuit breakers and bushings. This eliminates the need for bulky stand-alone devices for current measurement. Furthermore, the output signals, in contrast to the power outputs of conventional inductive current transformers, are compatible with modern digital control and protection systems. For a review of optical current sensing techniques, see [1].

Applications in high-voltage substations often require sensor accuracy within  $\pm 0.2\%$  over a wide temperature range, typically from  $-40^\circ\text{C}$  to  $85^\circ\text{C}$  [2]. Mechanical perturbations should not disturb the signal in order to avoid erroneous triggering of substation protection circuits. In the past, the performance of fiber-optic current sensors was often severely limited by unacceptably high sensitivity to both temperature and vibration. The signal drifts with temperature were largely the result of stress-induced linear birefringence in the sensing coil. In recent years, considerable improvements have been achieved in this regard by thermal annealing of the fused silica fiber coil

[3] and by using flint glass fiber having low stress-optic coefficients [4]. Other approaches to suppress the disturbing effects of linear birefringence are based on twisted fiber [5], fiber alignment along a helical path [6], spun elliptically birefringent fiber [7], and electronic compensation techniques [8]. Polarimetric as well as interferometric schemes have been employed to measure the magneto-optic phase shifts [9], [10].

However, even a perfect fiber coil still exhibits the inherent temperature dependence of the Verdet constant, which is  $0.7 \times 10^{-4} \text{ }^\circ\text{C}^{-1}$  for fused silica fiber [11]. Hence, the signal varies by about 0.9% over the described temperature range, which is outside the tolerances of high precision sensor applications. In this paper, a method is presented that allows us to inherently compensate the temperature dependence of the Faraday effect in Sagnac and polarization-rotated reflection interferometers. The sensors are built with annealed sensing fiber and employ elliptical-core fiber phase retarders to generate the circular or elliptical waves counterpropagating or copropagating in the coil.

First, we review the two sensor configurations and describe the preparation and characterization of the annealed coil and the retarders. Then, we theoretically and experimentally show how to employ the small temperature dependence of adequately prepared retarders to balance the temperature dependence of the Verdet constant within 0.2% over a temperature span of  $120^\circ\text{C}$ . Finally, we investigate and compare the sensitivity to vibration of the two configurations at frequencies up to 500 Hz and accelerations up to 10 g. It is verified that the reflective sensor configuration is, to a high degree, immune to mechanical perturbations.

## II. SENSOR CONFIGURATIONS

Fig. 1 shows the Sagnac configuration of the sensor [10], [12]–[14]. Two circular polarizations with the same sense of rotation are counterpropagating in the sensing coil. (Deliberate deviations from circular polarization will be discussed in Section IV.) The magnetic field of the current induces a nonreciprocal phase shift between the two waves given by

$$\Delta\phi_S = 2\varphi_F \quad (1)$$

with  $\varphi_F = VNI$ . Here,  $V$  is the Verdet constant of the fused silica fiber ( $2.65 \text{ } \mu\text{rad}/\text{A}$  at  $820 \text{ nm}$  [15]),  $N$  is the number of fiber loops, and  $I$  is the electric current. The circular polarizations are generated from linear polarizations prior to entering the coil by means of two short sections of elliptical-core fiber acting as quarter-wave retarders [16]. Upon leaving the coil, the circular waves are converted back to linear ones. Polarization-maintaining elliptical-core fibers serve to transmit the

Manuscript received July 19, 2001; revised October 22, 2001.

The authors are with ABB Corporate Research, Ltd., Baden-Dättwil CH-5405, Switzerland (e-mail: klaus.bohnert@ch.abb.com).

Publisher Item Identifier S 0733-8724(02)00690-4.

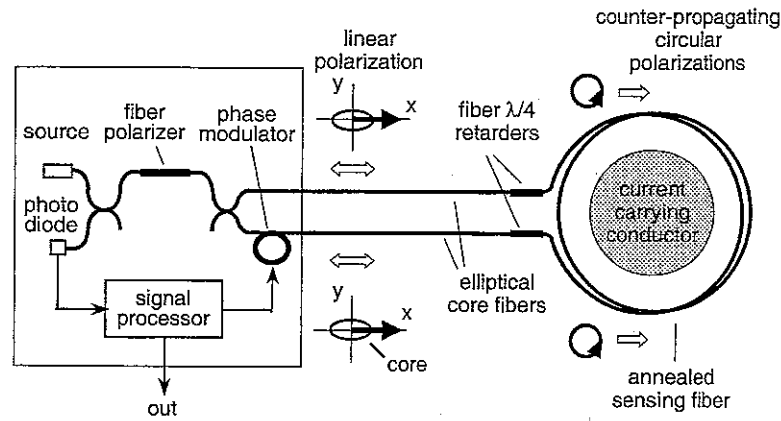


Fig. 1. Sagnac interferometer fiber-optic current sensor.

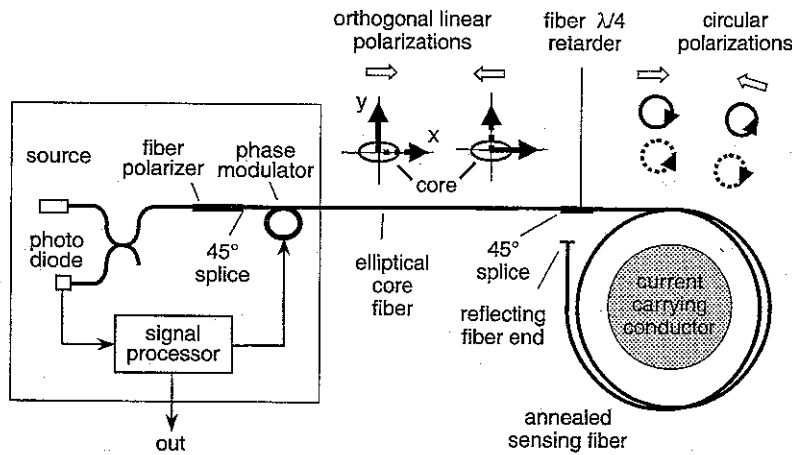


Fig. 2. Reflective fiber-optic current sensor.

forward- and backward-propagating linear waves. The polarization directions of the linear waves coincide and are for example parallel to the major core axis as indicated in Fig. 1. The broad-band semiconductor light source has a center wavelength  $\lambda$  near 820 nm. The scheme used to measure the current-induced optical phase shifts is identical to that of an open-loop minimum configuration fiber gyroscope [17]. Without further measures, the detected intensity resulting from the interference of the two returning linear waves is given by

$$I_d = I_o(1 + \cos \Delta\phi_S) \quad (2)$$

where  $I_o$  is proportional to the laser diode optical power. By means of nonreciprocal phase modulation [17], an output is generated that, for sufficiently small  $\Delta\phi_S$ , changes linearly with  $\Delta\phi_S$ . Here, the modulator is a disk-type or tube-type piezoelectric ceramic (pzt) with a number of fiber turns wrapped around it. The pzt is driven at its resonant frequency and modulates the differential phase of the two interfering waves with an amplitude  $\alpha_o$  of 1.84 rad. The current-induced phase shift  $\Delta\phi_S$  is then determined from the signal components  $I_d(\nu_m)$  and  $I_d(2\nu_m)$  at the first and second harmonics of the modulation frequency  $\nu_m$  as follows:

$$I_d(\nu_m)/I_d(2\nu_m) = [(J_1(\alpha_o)/J_2(\alpha_o)) \tan(\Delta\phi_S)]. \quad (3)$$

$J_1$  and  $J_2$  are the first- and second-order Bessel functions, respectively. With a modulation amplitude  $\alpha_o = 1.84$  rad,  $J_1(\alpha_o)$  is at its first maximum, which ascertains the maximum

signal-to-noise ratio. An alternating current of frequency  $\nu_{ac}$  gives rise to two side band signals at frequencies  $\nu_m \pm \nu_{ac}$ . For  $\Delta\phi_S \ll 1$  rad, the relationship between  $I_d(\nu_m)/I_d(2\nu_m)$  and  $\Delta\phi_S$  is approximately linear, and given by

$$I_d(\nu_m)/I_d(2\nu_m) = [(J_1(\alpha_o)/J_2(\alpha_o))\Delta\phi_S]. \quad (4)$$

A sensor output that is linear over a wider range can be achieved by digital signal processing.

In the polarization-rotated reflection interferometer also known as inline configuration [18]–[20], [14], the transmission direction of the fiber polarizer is at  $45^\circ$  with respect to the birefringent axes,  $x$  and  $y$ , of the elliptical-core fiber lead. Thus, two waves with orthogonal linear polarizations copropagate toward the sensing coil (Fig. 2). Prior to entering the coil, the linear polarizations are converted into left and right circular polarizations, again by an elliptical-core fiber retarder. At the coil end, the circular lightwaves are reflected and pass the coil a second time. Upon reflection, the polarizations are swapped, i.e., left circular turns into right circular polarization and vice versa. The quarter-wave retarder converts the returning circular waves back to orthogonal linear waves. Compared to the forward-traveling linear waves, the new polarization directions are also interchanged, i.e., the forward waves polarized along  $x$  and  $y$  become backward waves polarized along  $y$  and  $x$ , respectively. Finally, the two orthogonal waves are brought to interference in the fiber polarizer. As a result of the polarization

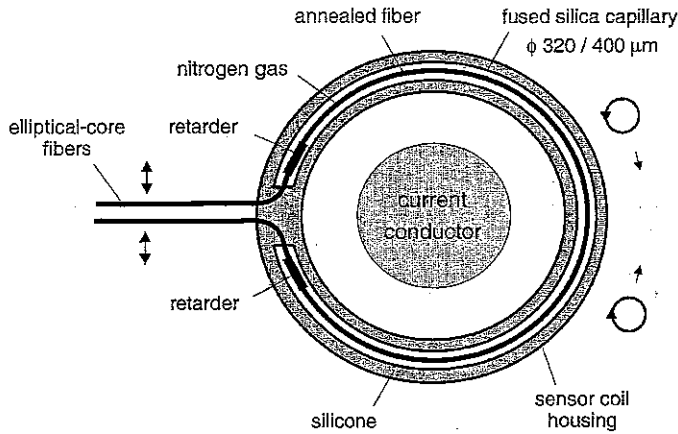


Fig. 3. The bare sensing fiber is residing and thermally annealed in a coiled capillary of fused silica (for clarity, only one loop is shown). The coil of capillary is embedded in silicone within a sealed housing.

swapping, the overall accumulated optical path imbalance of the interfering waves is zero. The current-induced nonreciprocal phase shift of the two waves is twice as large as in the Sagnac configuration

$$\Delta\phi_R = 4\phi_F. \quad (5)$$

The nonreciprocal phase modulator of the reflective configuration modulates the birefringence of the polarization maintaining fiber lead and thus the differential phase of the two orthogonal waves. Because it is difficult to obtain a sufficiently large modulation depth (i.e., 1.84 rad) with elliptical-core fibers, a fiber section with stress-induced birefringence is used for the modulator.

Apart from the reduced number of components, the reflection configuration has the important benefit that it is highly immune to mechanical shock and vibration [14], [21]. In both sensor configurations, vibration-induced perturbations are, for the most part, common mode for the two interfering waves and, therefore, tend to cancel each other. In particular, in the reflection interferometer, the perturbation of the differential phase of the forward-propagating waves is largely canceled on the return trip as a consequence of the polarization swapping. Remaining dynamic disturbances of the sensor signals are mainly due to the relative time delay between the two counterpropagating waves (Sagnac sensor) or the forward- and backward-propagating waves (reflective sensor) at a given location along the fiber. However, the differential phase of the two orthogonal waves of the reflective sensor is disturbed by about a factor of 1000 less than the phases of the two individual waves of the Sagnac sensor. Therefore, disturbances that can be observed in the Sagnac configuration are mostly negligible in the reflective configuration. Furthermore, in contrast to the Sagnac configuration, the reflective sensor is insensitive to rotational movements of the fiber coil (Sagnac effect).

### III. FIBER COIL AND RETARDERS

Fig. 3 illustrates the packaging of the sensing fiber coil (shown here for a coil operated in transmission). The bare

sensing fiber, with low intrinsic birefringence, 80- $\mu\text{m}$  outer diameter, and retarders at both ends, resides in a coiled capillary of fused silica. The inner and outer capillary diameters are 320 and 400  $\mu\text{m}$ , respectively. For clarity, only one fiber loop is shown in Fig. 3. Note that, in reality, the quarter-wave retarders are positioned next to each other so that a fully closed coil results. The coil is thermally annealed to eliminate the bend-induced mechanical stress [3]. The capillary is filled with dry nitrogen and embedded in silicone inside a sealed ring-shaped housing (see Fig. 4). A perturbation of the circular polarization states by mechanical stress and, hence, a deterioration of the sensor precision is avoided in a simple and reliable manner. The residual birefringent phase retardation in the sensing fiber after annealing is typically between 2° and 6° and is almost independent of temperature (Fig. 5). The coils investigated had up to 15 fiber loops and diameters of 137 and 117 mm.

As mentioned previously, the quarter-wave retarders are short sections of elliptical-core fiber with the birefringent axes at 45° with respect to the axes of the elliptical-core fiber leads and a length corresponding to a quarter of the fiber beat length [16]. Here, the beat length is about 3 mm. Fig. 6 illustrates an efficient procedure to manufacture the retarders. The method does not require active core axis alignment and accurate fiber cleaving to a defined length. A piece of elliptical-core fiber is fusion spliced to the low-birefringent sensing fiber. Subsequently, the two fused fiber sections are twisted by 45°. The twisted fiber stretch is typically about 5 cm in length. Next, the elliptical-core fiber section is heated in the arc of the splicer at a position separated from the splice by the proper length of the retarder. With adequate translation equipment, this position can be adjusted with a precision of a few micrometers. At the heated location, the fiber softens and the twist relaxes, resulting in the desired 45° angular offset in the core orientation. Although the offset is not abrupt—core imaging shows that the axis rotation takes place over a length of 500  $\mu\text{m}$ —perfect circular polarization can almost be achieved. As a consequence of the nonzero length of the rotation zone, the overall length of a 90° retarder is somewhat larger than it would be in the undisturbed fiber.

It was found that it is advantageous to prepare the retarder with a little overlength and approach the desired retardation by fine tuning the birefringence. To this purpose, the retarder section itself is heated in the arc of the splicer. This causes the Ge dopants in the core to partially diffuse out into the cladding and results in a reduction of the birefringence [22]. An additional mechanism may be a change in the intrinsic fiber stress induced by the heating. By successive short-time heating, the retardation can be reduced in a controlled manner by at least 25°. The procedure proved to be very useful for the implementation of the inherent temperature compensation discussed here.

Elliptical-core fiber retarders are advantageous in that retardation changes with temperature are relatively small. The retardation  $\rho$  of a 93.5° retarder made from such a fiber was found to decrease essentially linearly at a rate of  $\delta\rho/\delta T = (-2.05^\circ \pm 0.1^\circ) \times 10^{-2} \text{ }^\circ\text{C}^{-1}$  or  $(1/\rho)\delta\rho/\delta T = (-2.2 \pm 0.1) \times 10^{-4} \text{ }^\circ\text{C}^{-1}$  at 816 nm (Fig. 7). In contrast, the temperature dependence of fibers with stress-induced birefringence is larger by roughly an order of magnitude [23].

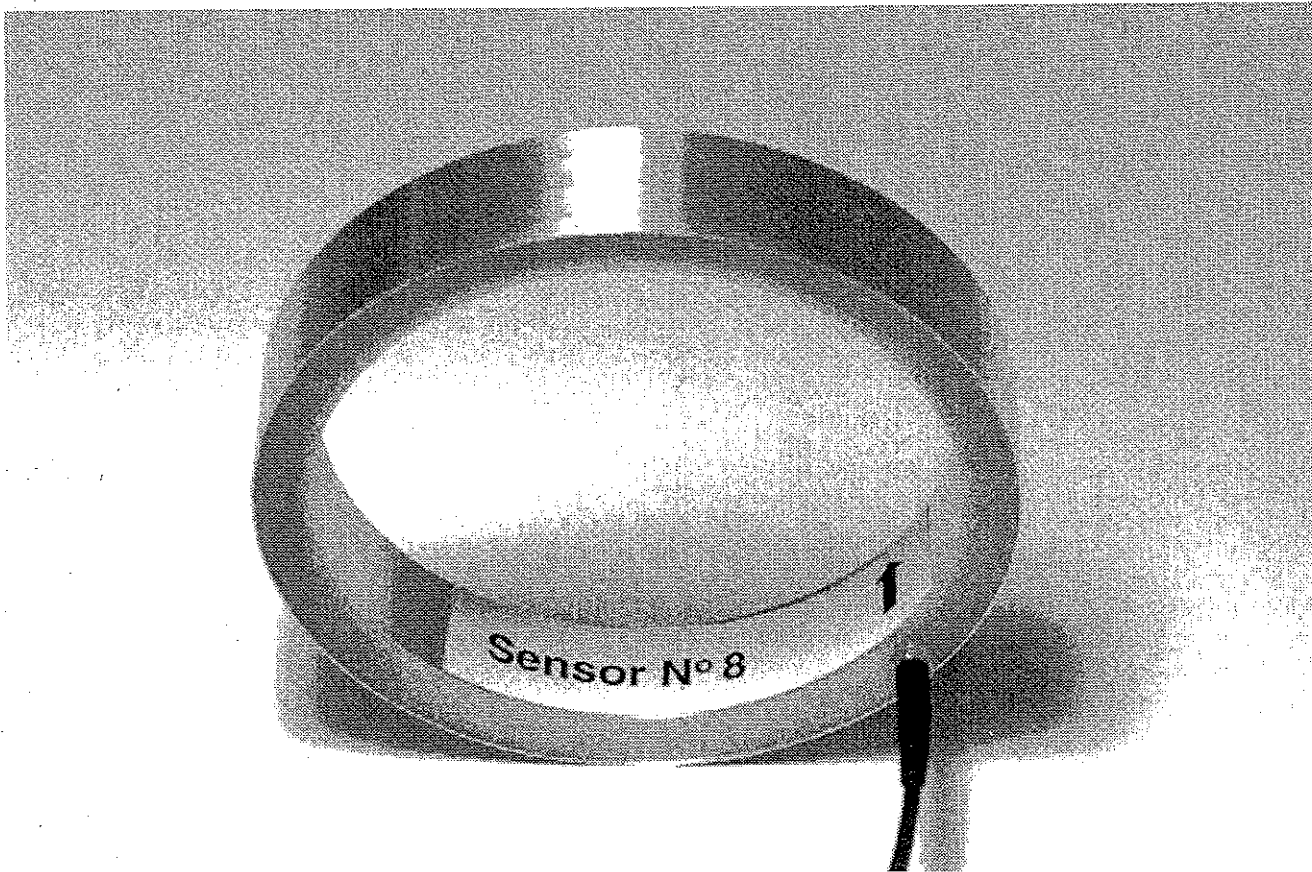


Fig. 4. Photograph of coil housing.

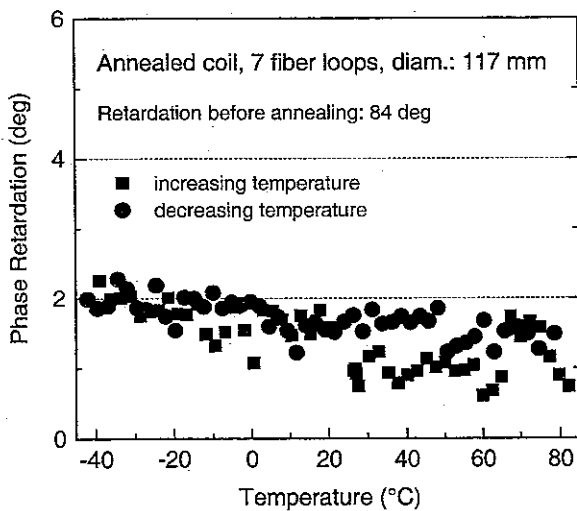


Fig. 5. Residual birefringence of sensor fiber coil (without retarders) versus temperature after thermal annealing. The birefringent phase retardation before annealing was about 84°.

#### IV. INHERENT TEMPERATURE COMPENSATION OF THE FARADAY EFFECT

We use the temperature dependence of the quarter-wave retarders and its effect on the scale factor, i.e., on the sensitivity of the sensor, to inherently compensate the variation of the Verdet constant with temperature. Nonperfect quarter-wave retarders (that is, retarders with retardations deviating from  $\pi/2$ ) have

been discussed by Frosio *et al.* [19], [20] and Short *et al.* [16]. In the following sections, the wave propagation in the two types of interferometer is analyzed in further detail, assuming retarders of varying retardations, and then it is shown both theoretically and experimentally how the retarders can be employed for temperature compensation.

##### A. Sagnac Configuration With Retarders of Varying Retardation

The simple relationships between  $\varphi_F$  (i.e., the current) and the observed phase shifts  $\Delta\phi_S$  and  $\Delta\phi_R$ , as given by (1) and (5), are valid only for circularly polarized light waves in the sensing coil, which presupposes retarders with true  $\pi/2$  phase retardation. If the retarders deviate from  $\pi/2$ —for example, as a result of temperature variations or manufacturing tolerances—the incoming linear polarizations are converted into elliptical ones. Each of the two elliptical polarizations counterpropagating in the coil of the Sagnac interferometer can be viewed as a superposition of two circular waves, namely, a main wave with the correct sense of rotation and an odd wave with opposite sense of rotation. The amplitudes of the main and odd waves vary in proportion to  $\cos(\varepsilon/2)$  and  $\sin(\varepsilon/2)$ , respectively, with  $\varepsilon$  being the deviation of the retarders from  $\pi/2$ . Another nonperfect quarter-wave retarder at the exit of the coil converts any of these circular waves into a polarization state that can be considered as a superposition of two orthogonal linear polarizations with directions parallel to the major and minor core axes of the exit fiber lead. The amplitudes of these orthogonal waves are

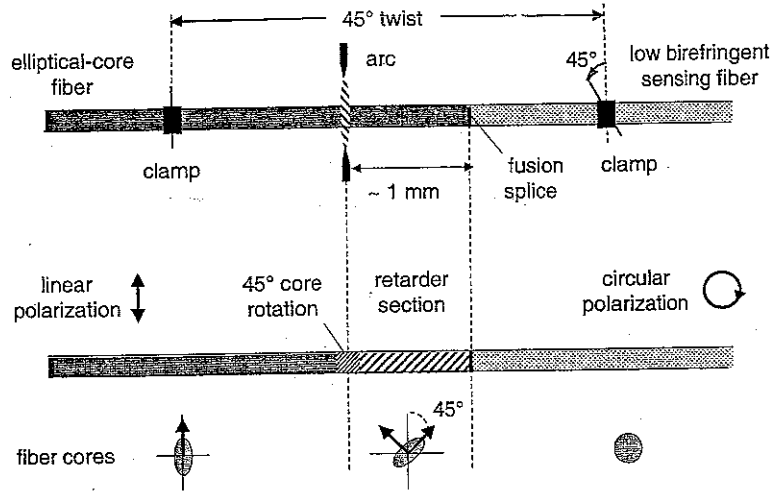
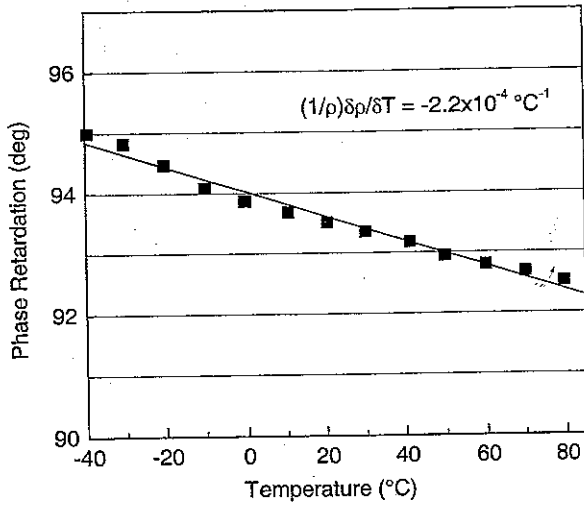


Fig. 6. Quarter-wave retarder manufacturing procedure.

Fig. 7. Phase retardation  $\rho$  of elliptical-core fiber retarder versus temperature.

obtained by again multiplying the amplitudes of their circular parent waves with  $\cos(\varepsilon/2)$  and  $\sin(\varepsilon/2)$ , respectively.

The complex amplitudes, including the phases, of the waves returning from the coil are obtained from a Jones matrix description of the light propagation [24], [19], [16]. In the Sagnac configuration, we define the directions of the birefringent axes of the elliptical core fiber leads as  $x$  and  $y$ . We further assume that the polarizer is aligned along  $x$ , and take as unity the amplitudes of the two linear waves propagating in clockwise (cw) and counterclockwise (ccw) directions toward the coil. In the ideal case of true  $\pi/2$  retarders, the amplitudes of the returning waves with polarizations along  $x$  and  $y$  are then simply given as

$$E_{x, cw} = i \exp[i(\chi - \varphi_F)] \quad (6a)$$

$$E_{x, ccw} = i \exp[i(\chi + \varphi_F)] \quad (6b)$$

$$E_{y, cw} = 0 \quad (6c)$$

$$E_{y, ccw} = 0 \quad (6d)$$

with  $\varphi_F = VNI$ .  $\chi$  is the angle between the fast axes of the retarders. Optical losses are neglected and the coil is assumed to be free of linear and, in the absence of a current, circular birefringence. Phase terms introduced by the nonreciprocal phase

modulator are omitted here (without limiting the validity of the considerations) and will be addressed in Section IV-C. If the two retarders deviate from  $\pi/2$  by the amounts  $\varepsilon_1$  and  $\varepsilon_2$ , respectively, one obtains instead

$$E_{x, cw} = i \cos(\varepsilon_1/2) \cos(\varepsilon_2/2) \exp[i(\chi - \varphi_F)] - i \sin(\varepsilon_1/2) \sin(\varepsilon_2/2) \exp[-i(\chi - \varphi_F)] \quad (7a)$$

$$E_{x, ccw} = i \cos(\varepsilon_2/2) \cos(\varepsilon_1/2) \exp[i(\chi + \varphi_F)] - i \sin(\varepsilon_2/2) \sin(\varepsilon_1/2) \exp[-i(\chi + \varphi_F)] \quad (7b)$$

$$E_{y, cw} = -\cos(\varepsilon_1/2) \sin(\varepsilon_2/2) \exp[i(\chi - \varphi_F)] - \sin(\varepsilon_1/2) \cos(\varepsilon_2/2) \exp[-i(\chi - \varphi_F)] \quad (7c)$$

$$E_{y, ccw} = -\cos(\varepsilon_2/2) \sin(\varepsilon_1/2) \exp[i(\chi + \varphi_F)] - \sin(\varepsilon_2/2) \cos(\varepsilon_1/2) \exp[-i(\chi + \varphi_F)]. \quad (7d)$$

Each of the two returning linear waves along  $x$ ,  $E_{x, cw}$ , and  $E_{x, ccw}$  whose interference signal is detected can also be viewed as a superposition of a main and an odd linear wave. In the special case of  $\varepsilon_1 = \varepsilon_2 = \varepsilon$ , the amplitudes of the two main waves are reduced by a factor of  $\cos^2(\varepsilon/2)$  compared to the case of true  $\pi/2$  retarders. The odd wave amplitudes increase in proportion to  $\sin^2(\varepsilon/2)$ . The phase of the odd waves with respect to the main waves depends on the relative alignment of the fast axes of the two retarders. At zero current, the odd waves are in phase with the main waves for orthogonal alignment ( $\chi = 90^\circ$ ) and are opposite in phase for parallel alignment ( $\chi = 0^\circ$ ). The nonreciprocal differential Faraday phase shift of the main waves is  $2\varphi_F$ . The odd waves experience an equal shift, but of opposite sign. The waves returning with polarizations along  $y$ , i.e.,  $E_{y, cw}$  and  $E_{y, ccw}$ , are orthogonal to the transmission direction of the polarizer and are therefore not detected. Note that the phase delays between  $x$  and  $y$  polarizations as a result of the birefringence of the fiber leads are not considered in (6) and (7) because, other than in the reflective configuration, they have no effect in the Sagnac configuration.

The phase difference between  $E_{x, cw}$  and  $E_{x, ccw}$  can be written as

$$\Delta\phi_S = \arctan \frac{(\cos \varepsilon_1 + \cos \varepsilon_2) \sin 2\varphi_F}{(1 + \cos \varepsilon_1 \cos \varepsilon_2) \cos 2\varphi_F - \sin \varepsilon_1 \sin \varepsilon_2 \cos 2\chi} \quad (8)$$

In the special case of small Faraday phase shifts  $\varphi_F$  and equal retarders, i.e.,  $\varepsilon_1 = \varepsilon_2 = \varepsilon$ , the nonreciprocal phase difference for parallel and perpendicular retarders is approximated by

$$\Delta\phi_S = 2\varphi_F / \cos \varepsilon, \quad \chi = 0^\circ \quad (9a)$$

and

$$\Delta\phi_S = 2\varphi_F \cos \varepsilon, \quad \chi = 90^\circ. \quad (9b)$$

For small  $\varepsilon$ , (9a) and (9b) further reduce, in agreement with [16], [19], to  $\Delta\phi_S = 2\varphi_F(1 \pm \varepsilon^2/2)$  with the plus and minus signs referring to parallel and orthogonal retarders, respectively. In the case of a  $45^\circ$  angle between the fast retarder axes,  $\Delta\phi_S$  is given by  $\Delta\phi_S = 2\varphi_F(1 - \varepsilon^4/8)$  [16].

The detected intensity resulting from the superposition of  $E_{cw}^{(x)}$  and  $E_{ccw}^{(x)}$  can be written as

$$I_d = (I_0/2) \cos^2 \varphi_F (\sin^2 \chi + \cos^2 \varepsilon \cos^2 \chi). \quad (10)$$

### B. Reflection Configuration with Retarders of Varying Retardation

The amplitudes of the forward-propagating linear waves, now with polarizations along  $x$  and  $y$ , are again assumed as unity. In the case of a true  $\pi/2$  retarder, the amplitudes of the returning linear waves are given by

$$E_x = i \exp(-i2\varphi_F) \quad (11a)$$

$$E_y = i \exp(i2\varphi_F). \quad (11b)$$

If the retarder deviates by  $\varepsilon$  from  $\pi/2$ , one obtains

$$E_x = i \cos^2(\varepsilon/2) \exp(-2i\varphi_F) - i \sin^2(\varepsilon/2) \cdot \exp(2i\varphi_F) - \cos(\varepsilon/2) \sin(\varepsilon/2) \cdot [\exp(i(\Delta\theta + 2\varphi_F)) + \exp(i(\Delta\theta - 2\varphi_F))] \quad (12a)$$

$$E_y = i \cos^2(\varepsilon/2) \exp(2i\varphi_F) - i \sin^2(\varepsilon/2) \cdot \exp(-2i\varphi_F) - \cos(\varepsilon/2) \sin(\varepsilon/2) \cdot [\exp(-i(\Delta\theta + 2\varphi_F)) + \exp(-i(\Delta\theta - 2\varphi_F))]. \quad (12b)$$

The first two terms in (12a) and (12b) describe the coherent waves returning with swapped polarizations, i.e., polarizations orthogonal to those of their forward-propagating parent waves. The third and fourth terms represent the waves returning with unswapped polarizations. The corresponding waves in the Sagnac configuration return with polarizations along  $y$  and are blocked by the polarizer. As a result of the birefringence of the elliptical-core fiber, the unswapped waves accumulate optical path imbalances  $\pm\Delta L = \pm\Delta n_g L$  with respect to the swapped waves. Here,  $\Delta n_g$  is the group index difference between the orthogonal polarizations and  $L$  is the length of the elliptical-core fiber lead. The path imbalances are much longer than the coherence length of the broad band source and, therefore, the unswapped waves interfere incoherently and have no effect on the recovered nonreciprocal phase shift. The phase differences  $\pm\Delta\theta$  associated with these path imbalances are given by  $\Delta\theta = 2\pi\Delta n L/\lambda$ , with  $\Delta n$  representing the birefringence of the elliptical-core fiber.

The current-induced phase difference  $\Delta\phi_R$  between the coherent terms of  $E_x$  and  $E_y$  is, apart from the doubled Faraday phase term ( $4\varphi_F$  instead of  $2\varphi_F$ ), the same as the one in the

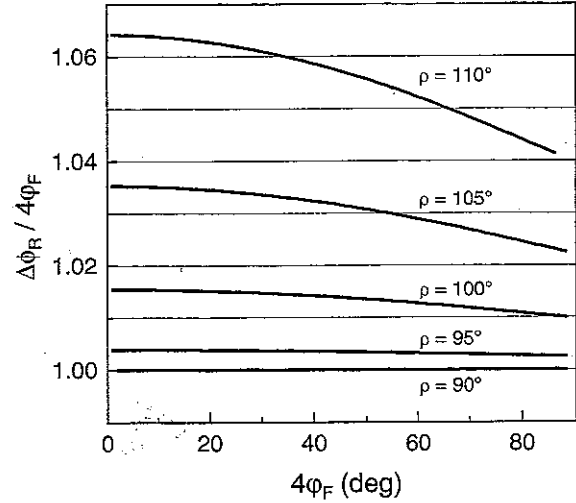


Fig. 8. Normalized scale factor (sensitivity of sensor)  $\Delta\phi_R/4\varphi_F$ , according to (13) as a function of the Faraday phase shift  $4\varphi_F$  for various retardations  $\rho$  of the retarder (reflective sensor configuration). If  $4\varphi_F$  is replaced by  $2\varphi_F$ , the curves are also valid for the Sagnac configuration with parallel alignment of the fast retarder axes.

Sagnac configuration with identical parallel retarders ( $\varepsilon_1 = \varepsilon_2 = \varepsilon$ ,  $\chi = 0^\circ$ ) as follows:

$$\Delta\phi_R = \arctan \frac{2 \cos \varepsilon \sin 4\varphi_F}{(1 + \cos^2 \varepsilon) \cos 4\varphi_F - \sin^2 \varepsilon}. \quad (13)$$

For small Faraday phase shifts,  $\varphi_F$ , the phase difference can be approximated analogously to the Sagnac configuration as

$$\Delta\phi_R = 4\varphi_F / \cos \varepsilon. \quad (14)$$

In general, the detected intensity is given by

$$I_d = (I_0/2) \cos^2 2\varphi_F \cdot [\cos^2 \varepsilon + (1/2) \sin^2 \varepsilon (1 + |\gamma(2\Delta L)| \cos(4\pi L \Delta n / \lambda))]. \quad (15)$$

The term governed by  $\sin^2 \varepsilon$  is due to the unswapped waves. It depends on their degree of coherence,  $|\gamma(2\Delta L)|$ , and oscillates in case of, e.g., thermal variations in the birefringence  $\Delta n$  and the length  $L$  of the elliptical-core fiber lead. With a low coherent source,  $|\gamma(2\Delta L)|$  is essentially zero and (15) reduces to

$$I_d = (I_0/2) \cos^2 2\varphi_F [\cos^2 \varepsilon + (1/2) \sin^2 \varepsilon]. \quad (16)$$

Apart from the term  $(I_0/4) \cos^2 2\varphi_F \sin^2 \varepsilon$ , which describes the intensity of the incoherent light, (16) is equivalent to (10) for the Sagnac configuration with  $\chi = 0$ .

It is obvious from (8) and (13) that the relationship between the recovered phase shifts  $\Delta\phi_{S,R}$  and the Faraday phase shift  $\varphi_F$  of a sensor with imperfect  $\pi/2$  retarders, i.e., with  $\varepsilon \neq 0$ , is nonlinear (Fig. 8). Although the nonlinearity strongly increases with increasing  $\varepsilon$  and  $\varphi_F$ , it can be neglected in many practical cases. For example, for a reflective sensor with a  $100^\circ$  retarder, as discussed here, the error remains below 0.2% as long as  $\Delta\phi_R$  does not exceed  $50^\circ$ .

The scale factor also changes if the angle between the birefringent axes of the elliptical-core fiber leads and the retarders deviates by an amount  $\Delta\beta$  from a perfect  $45^\circ$  orientation [19], [16]. For a given  $\varepsilon$ , the signal decreases in proportion to  $\cos(2\Delta\beta)$ , if  $\Delta\beta$  and  $\varepsilon$  are small. For small  $\varphi_F$  and arbitrary

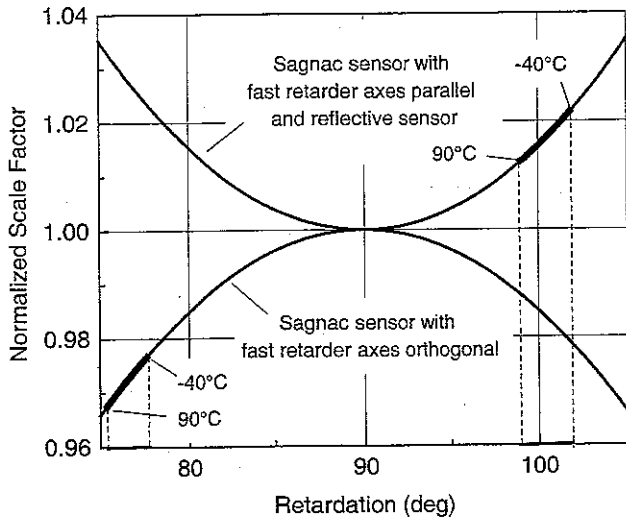


Fig. 9. Variation of normalized scale factor (sensitivity of sensor) with phase retardation  $\rho$  of the retarders (adapted from [19], [20], [16]) and application to temperature compensation of Verdet constant. The heavy curve segments indicate the variation in sensitivity due to the temperature dependence of the retarders having a room temperature retardation of  $100.4^\circ$  (upper branch) and  $76.5^\circ$  (lower branch) and a temperature coefficient  $(1/\rho)\delta\rho/\delta T = -2.2 \times 10^{-4} \text{ }^\circ\text{C}^{-1}$ . The resulting variations in sensitivity compensate the change of the Verdet constant with temperature (see Fig. 10).

$\Delta\beta$  and  $\varepsilon$ , the nonreciprocal phase shift in the reflective sensor is given by

$$\Delta\phi_R = \frac{\cos \varepsilon \cos(2\Delta\beta)}{\cos^2 \varepsilon + \sin^2 \varepsilon \sin^2(2\Delta\beta)} 4\phi_F. \quad (17)$$

### C. Nonreciprocal Phase Modulation With Retarders of Varying Retardation

With nonreciprocal phase modulation  $\alpha = \alpha_0 \sin(2\pi\nu_m t)$ , the detected intensity in the Sagnac configuration is given by

$$I_d = (I_0/2) \{ \sin^2 \chi [\cos(\alpha/2) \cos \varphi_F + \sin(\alpha/2) \sin \varphi_F \cos \varepsilon]^2 + \cos^2 \chi [\cos(\alpha/2) \cos \varphi_F \cos \varepsilon + \sin(\alpha/2) \sin \varphi_F]^2 \} \quad (18)$$

and the intensity in the reflection configuration is given by

$$I_d = (I_0/2) \{ [\cos(\alpha/2) \cos 2\varphi_F \cos \varepsilon + \sin(\alpha/2) \sin 2\varphi_F]^2 + (1/2) \sin^2 \varepsilon \cos^2 2\varphi_F \}. \quad (19)$$

It can be shown that the components of  $I_d$  at the first and second harmonics of the modulation frequency  $\nu_m$  give, if inserted in (3), the current-induced phase shifts of (8) and (13). Therefore, the considerations in Sections IV-A and IV-B remain valid in case of signal recovery based on a nonreciprocal phase modulation scheme.

### D. Application to Inherent Temperature Compensation

Fig. 9 shows the normalized sensitivities for the two sensor configurations as a function of the phase delay of the retarders,  $\rho = \pi/2 + \varepsilon$ , according to (9a), (9b), and (14); see also [19], [20], [16]. The normalized sensitivities are defined as the ratios  $\Delta\phi_S/2\varphi_F$  and  $\Delta\phi_R/4\varphi_F$ , respectively. The temperature dependence of the retarders and its effect on the sensitivity is now employed to compensate the temperature dependence of the Verdet constant. Considering the Sagnac configuration with

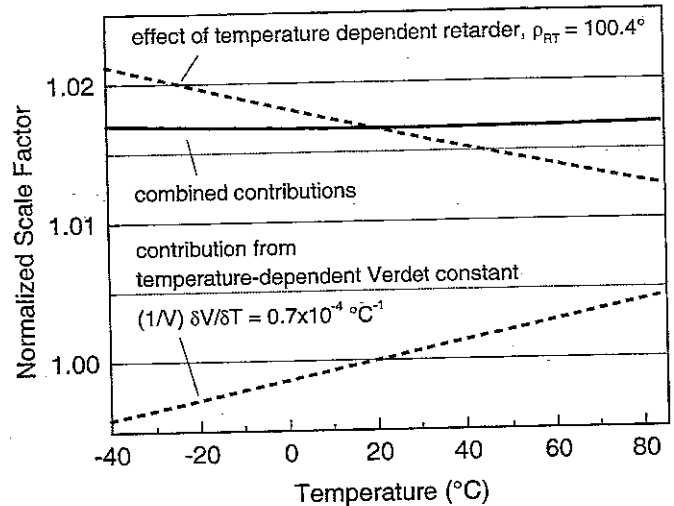


Fig. 10. Individual contributions of Verdet constant and adequately prepared retarders to temperature dependence of scale factor (Sagnac configuration with parallel retarders and reflective sensor). The combined contributions result in a temperature-independent sensitivity. The temperature dependence of the retardation  $\rho$  of  $(1/\rho)\delta\rho/\delta T = -2.2 \times 10^{-4} \text{ }^\circ\text{C}^{-1}$  requires the setting of the room temperature retardation  $\rho_{RT}$  to  $100.4^\circ$  to compensate the temperature dependence of the Verdet constant  $V$  of  $(1/V)\delta V/\delta T = 0.7 \times 10^{-4} \text{ }^\circ\text{C}^{-1}$ .

parallel alignment of the identical retarders or, equivalently, the reflection configuration and assuming retarders with a temperature dependence as shown in Fig. 7, we set the room temperature retardation to  $100.4^\circ$  rather than  $90^\circ$ . The heavy curve segment on the upper branch in Fig. 9 then indicates the variation in sensitivity as a result of the change in retardation with temperature. This variation in sensitivity just offsets the temperature dependence of the Verdet constant, as depicted in Fig. 10. It is clear from Fig. 9 that room temperature retardations larger than  $100.4^\circ$  result in overcompensation, whereas those smaller than  $100.4^\circ$  result in undercompensation or even an enhanced temperature dependence if the retardation is chosen below  $90^\circ$ . The room temperature retardation must be between  $98.4^\circ$  and  $102.2^\circ$  if the residual temperature dependence of the sensor is to be kept within  $\pm 0.2\%$  over a temperature range of  $125^\circ\text{C}$  ( $-40$  to  $85^\circ\text{C}$ ). Temperature compensation of the Sagnac configuration with orthogonal retarders of equal delays requires retardations of  $76.5^\circ$  (heavy segment on lower branch). Note that the absolute change  $\delta\rho$  in retardation decreases with  $\rho$ .

The compensation scheme is rather straightforward to implement for the reflective sensor because only the retardation of a single retarder must be adjusted. In contrast, in the Sagnac configuration, both the retardations and relative angular orientation of two retarders must be properly set.

In order to verify the concept, several reflective current sensors were prepared with retarders having phase delays between  $60^\circ$  and  $109^\circ$  at room temperature. The sensor signals were measured as a function of the retarder temperature for an alternating current of constant amplitude. The retarder temperature was varied between room temperature and  $100^\circ\text{C}$  with a precision of  $0.2^\circ\text{C}$  by exposing the retarder to an air stream of controlled temperature. The sensing fiber was kept at room temperature. For simplicity, the fiber was aligned straight and placed into the magnetic field inside a solenoid. Fig. 11 compares the experimental signals [recovered root mean square

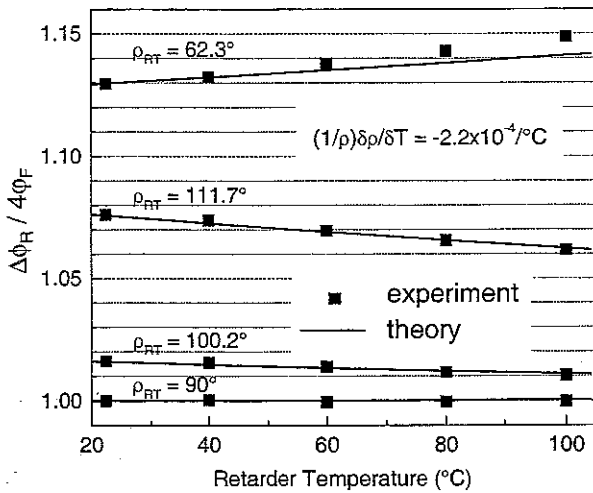


Fig. 11. Experimental and theoretical sensor signals (reflective current sensor) as a function of the retarder temperature. The temperature of the sensing fiber was kept constant. The four data sets correspond to sensors having retarders with room temperature retardations  $\rho_{RT}$  of about  $90^\circ$ ,  $100^\circ$ ,  $112^\circ$ , and  $62^\circ$ . The theoretical curves were calculated according to (13) using the measured temperature dependence of the retardation of  $(1/\rho)\delta\rho/\delta T = -2.2 \times 10^{-4}/^\circ\text{C}$ . The  $100^\circ$  retarder results in a slope of  $-0.63 \times 10^{-4}/^\circ\text{C}$ , which largely cancels the temperature dependence of the Verdet constant.

(rms) optical phase shifts] with theory, i.e., with the normalized sensitivity,  $\Delta\phi_R/4\phi_F$ , according to (13). The experimental data points were normalized with a common factor such that the signal at a retardation of  $90^\circ$  corresponded to unity. The theoretical curves were computed using the experimentally determined temperature dependence of the retardation  $\rho$  of  $(1/\rho)\delta\rho/\delta T = -2.2 \times 10^{-4}/^\circ\text{C}$  from Fig. 7 and treating the room temperature phase delays of the retarders as adjustable parameters. The resulting retardations of  $90.0^\circ$ ,  $100.2^\circ$ ,  $111.7^\circ$ , and  $62.3^\circ$  agree well with the experimentally measured retardations, which were  $90^\circ$ ,  $101^\circ$ ,  $109^\circ$ , and  $60^\circ$ , respectively, with an uncertainty of about  $\pm 1.5^\circ$ . Also, the variations in the experimental and theoretical sensitivities with retarder temperature are in good agreement. Some noticeable deviations in the case of the  $62^\circ$  retarder are attributed to its short length. Here, modifications of the fiber properties caused by splicing are more pronounced. It should be mentioned that the  $101^\circ$  and  $90^\circ$  retarders were obtained from the  $109^\circ$  retarder (with  $1050 \mu\text{m}$  in length) by consecutively reducing the retardation by fine tuning, as described in Section III.

By varying the temperature of the sensing fiber while keeping the retarder at constant temperature, we determined the temperature dependence of the Verdet constant. We found  $(1/V)dV/dT = (0.75 \pm 0.25) \times 10^{-4}/^\circ\text{C}$ , which is consistent with published data [11].

Finally, a reflective sensor was prepared with an annealed coil (two loops) and a retarder (added after annealing of the coil) whose retardation was set for temperature compensation of the Faraday effect. A variation of only the retarder temperature (between 22 and  $100^\circ\text{C}$ ) changed the normalized signal at a rate of  $(-0.7 \pm 0.1) \times 10^{-4}/^\circ\text{C}$ . Fig. 12 shows the signal as a function of the coil temperature (common temperature of retarder and sensing fiber) between  $-35$  and  $85^\circ\text{C}$ . The signal remains constant, well within  $\pm 0.2\%$ , as required in demanding

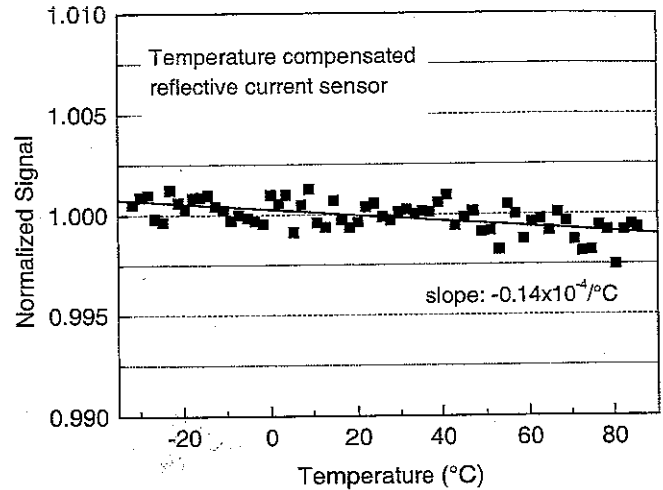


Fig. 12. Signal versus coil temperature for a temperature-compensated reflective current sensor.

high-voltage substation applications. The slight overcompensation ( $-0.14 \times 10^{-4} \text{ }^\circ\text{C}^{-1}$ ) is consistent with the tolerances of the retarder manufacturing and the uncertainty in the temperature coefficient of the Verdet constant.

## V. SENSITIVITY TO VIBRATION

The excellent performance of the reflective sensor under mechanical vibrations has been already reported in [21]. Here, we further confirm these findings by a direct comparison of the Sagnac and reflective configurations. The packaged sensor coils were mounted on a vibration table and subjected to harmonic accelerations of up to 10 g at frequencies up to 500 Hz. The accelerations were applied parallel and perpendicular to the plain of the coil. The coil of the Sagnac sensor had nine fiber loops, the coil of the reflective sensor had two loops (which is equivalent to a Sagnac sensor with four loops). Note, however, that the vibration-induced signal in terms of equivalent current should be approximately independent of the number of fiber loops.

The outstanding performance of the reflection configuration is seen in Fig. 13, where the sensitivity to vibration (here, excitation parallel to the plane of the coil) of the two sensors is compared in the range 20–500 Hz at an acceleration of 5 g. The Sagnac sensor shows vibration-induced signals corresponding to about 5 A rms (disregarding the peaks due to uncontrolled resonant table vibrations perpendicular to the nominal vibration direction). For the reflective sensor, no vibration effects are seen, i.e., there is no noticeable difference in the recorded spectra with and without vibration. Note that the spectra were recorded by sweeping the vibration frequency and detecting the signal spectrum with a dynamic signal analyzer in a peak hold averaging mode. In the presence of detectable signals (Sagnac sensor), this procedure results in the rms amplitude spectrum of the sensor output. In the absence of detectable vibration signals, as in the case of the reflective sensor, the spectrum shows peak noise which occurred during the sweep period (a few minutes). The spectrum of the reflective sensor in Fig. 13 shows the difference of the recorded spectra (peak noise spectra) with and without vibration. Fig. 14 compares the vibration-induced rms

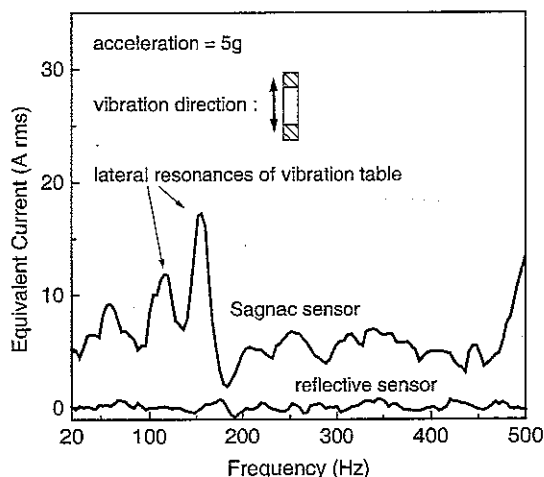


Fig. 13. Vibration-induced signals in terms of equivalent current versus vibration frequency for the Sagnac and reflective sensor configurations, respectively. The acceleration is 5 g.

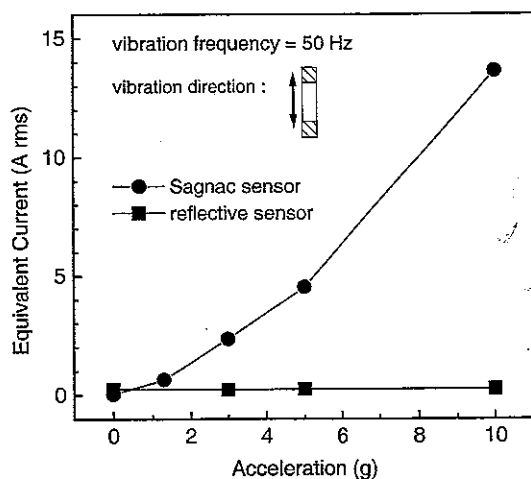


Fig. 14. Vibration-induced signals in terms of equivalent current for the Sagnac and reflective sensor configurations, respectively, as a function of acceleration. The vibration frequency is 50 Hz.

signals at a fixed frequency of 50 Hz as a function of the acceleration. Even at 10 g the reflective sensor was not affected by vibration, i.e., the signal perturbations corresponded to less than the noise equivalent current of about  $0.2 \text{ A rms}/\sqrt{\text{Hz}}$ . Similar results were obtained for vibrations perpendicular to the plane of the coil.

## VI. CONCLUSION

A robust temperature- and vibration-insensitive fiber-optic current sensor has been demonstrated. Sagnac and polarization-rotated reflection interferometer configurations of the sensor were considered. The sensing fiber is residing and thermally annealed in a capillary of fused silica. This makes simple packaging of the coil possible and prevents deterioration of the signal by temperature dependent linear birefringence. The birefringent phase retarders of the sensor, which generate the elliptical waves counter- or copropagating in the coil, consist of a short section of elliptical-core fiber. The  $45^\circ$  angular alignment of the retarder

axes with respect to the axes of the elliptical-core fiber lead is achieved by relaxation of a  $45^\circ$  fiber torsion in the arc of a fusion splicer. The retardation is fine tuned to the desired value by multiple short-time heating of the retarder in the splicer.

The optical wave propagation in the two interferometers for nonquarter-wave retarders was analyzed in detail. For small Faraday phase shifts, the sensitivity of the sensor varies in proportion to  $1/\cos \epsilon$ , with  $\epsilon$  being the deviation of the retardation  $\rho$  from  $\pi/2$ , both for the Sagnac configuration with parallel alignment of the fast retarder axes and for the reflective configuration. The sensitivity varies proportionally to  $\cos \epsilon$  for the Sagnac configuration with orthogonal alignment of the fast axes. The temperature dependence of the retardation was employed to inherently balance the temperature dependence of the Faraday effect ( $0.7 \times 10^{-4} \text{ }^\circ\text{C}^{-1}$ ). This requires setting of the room temperature retardation to an appropriately chosen value (here,  $100^\circ$ , in the case of the reflective sensor). Insensitivity of the sensor to temperature within 0.2% between  $-35$  and  $85 \text{ }^\circ\text{C}$  has been achieved. The nonlinearity in the signal-versus-current relationship, which occurs for  $\epsilon \neq 0$ , stays below 0.2% in the case of  $100^\circ$  retarders as long as the current-induced phase shift between the interfering waves does not exceed  $50^\circ$ .

In particular, the reflective sensor configuration was found to be undisturbed by vibrations of the coil at accelerations up to 10 g and frequencies up to 500 Hz. Thus, the sensor fulfills the essential requirements of the electrical power industry.

## REFERENCES

- [1] Y. N. Ning, Z. P. Wang, A. W. Palmer, K. T. V. Grattan, and D. A. Jackson, "Recent progress in optical current sensing techniques," *Rev. Sci. Instrum.*, vol. 66, no. 5, pp. 3097–3111, 1995.
- [2] "International standard for current transformers," International Electrotechnical Commission (IEC), Geneva, Switzerland, IEC 185, 1987.
- [3] D. Tang, A. H. Rose, G. W. Day, and S. M. Etzel, "Annealing of linear birefringence in single-mode fiber coils: Applications to optical fiber current sensors," *J. Lightwave Technol.*, vol. 9, pp. 1031–1037, Aug. 1991.
- [4] K. Kurosawa, S. Yoshida, K. Sakamoto, I. Masuda, and T. Yamashita, "An optical fiber-type current sensor utilizing the Faraday effect of flint glass fiber," in *Proc. Int. Conf. Optical Fibre Sensors*, vol. 2360, 1994, pp. 24–27.
- [5] R. Ulrich and A. Simon, "Polarization optics of twisted single-mode fibers," *Appl. Opt.*, vol. 18, no. 13, pp. 2241–2251, 1979.
- [6] F. Maystre and A. Bertholds, "Magneto-optic current sensor using a helical-fiber Fabry-Perot resonator," *Opt. Lett.*, vol. 14, no. 11, pp. 587–589, 1989.
- [7] R. I. Laming and D. N. Payne, "Electric current sensors employing spun highly birefringent optical fibers," *J. Lightwave Technol.*, vol. 7, pp. 2084–2094, Dec. 1989.
- [8] P. Menke and T. Bosselmann, "Temperature compensation in magneto-optic ac current sensors using an intelligent ac-dc signal evaluation," *J. Lightwave Technol.*, vol. 13, pp. 1362–1370, July 1995.
- [9] A. Papp and H. Harms, "Magneto-optical current transformer 1: Principles," *Appl. Opt.*, vol. 19, no. 22, pp. 3729–3734, 1980.
- [10] P. A. Nicatti and P. Robert, "Stabilized current sensor using a Sagnac interferometer," *J. Phys. E: Sci. Instrum.*, vol. 21, pp. 791–796, 1988.
- [11] P. A. Williams, A. H. Rose, G. W. Day, T. E. Milner, and M. N. Deeter, "Temperature dependence of the Verdet constant in several diamagnetic glasses," *Appl. Opt.*, vol. 30, no. 10, pp. 1176–1178, 1991.
- [12] G. Frosio, K. Hug, and R. Dändliker, "All-fiber Sagnac current sensor," in *Proc. Opto'92* Paris, France, 1992, pp. 560–564.
- [13] K. Bohnert, H. Brändle, and G. Frosio, "Field test of interferometric optical fiber high-voltage and current sensors," in *Proc. Int. Conf. Optical Fiber Sensors*, vol. 2360, 1994, pp. 16–19.
- [14] J. Blake, P. Tantaswadi, and R.T. de Carvalho, "In-line Sagnac interferometer current sensor," *IEEE Trans. Power Delivery*, vol. 11, pp. 116–121, Jan. 1996.

- [15] A. H. Rose, S. M. Etzel, and C. M. Wang, "Verdet constant dispersion in annealed optical fiber current sensors," *J. Lightwave Technol.*, vol. 15, pp. 803–807, July 1997.
- [16] S. X. Short, A. A. Tselikov, J. U. de Arruda, and J. N. Blake, "Imperfect quarter-waveplate compensation in Sagnac interferometer-type current sensors," *J. Lightwave Technol.*, vol. 16, pp. 1212–1219, July 1998.
- [17] R. A. Bergh, H. C. Lefevre, and H. J. Shaw, "An overview of fiber-optic gyroscopes," *J. Lightwave Technol.*, vol. LT-2, pp. 91–107, 1984.
- [18] A. Enokihara, M. Izutsu, and T. Sueta, "Optical fiber sensors using the method of polarization-rotated reflection," *J. Lightwave Technol.*, vol. 5, pp. 1584–1590, Nov. 1987.
- [19] G. Frosio, "Reciprocal interferometers for fiber-optic Faraday current sensors," Ph.D. dissertation, Univ. Neuchatel, Neuchatel, Switzerland, 1992.
- [20] G. Frosio and R. Dändliker, "Reciprocal reflection interferometer for a fiber-optic Faraday current sensor," *Appl. Opt.*, vol. 33, no. 25, pp. 6111–6122, 1994.
- [21] S. X. Short, P. Tantaswadi, R. T. de Carvalho, B. D. Russell, and J. Blake, "An experimental study of acoustic vibration effects in optical fiber current sensors," *IEEE Trans. Power Delivery*, vol. 11, pp. 1702–1706, Oct. 1996.
- [22] R. B. Dyott, private communication, 1998.
- [23] F. Zhang and J. W. Lit, "Temperature and strain sensitivity measurements of high-birefringent polarization maintaining fibers," *Appl. Opt.*, vol. 32, no. 13, pp. 2213–2218, 1993.
- [24] R. C. Jones, "A new calculus for the treatment of optical systems—Part I: Description and discussion of the calculus," *J. Opt. Soc. Amer.*, vol. 31, pp. 488–493, 1941.
- K. Bohnert**, photograph and biography not available at the time of publication.
- P. Gabus**, photograph and biography not available at the time of publication.
- J. Nehring**, photograph and biography not available at the time of publication.
- H. Brändle**, photograph and biography not available at the time of publication.